Journal of Computational and Applied Mathematics 424 (2023) 115005

Contents lists available at ScienceDirect

Journal of Computational and Applied Mathematics

journal homepage: www.elsevier.com/locate/cam

A FETD scheme and analysis for photonic crystal waveguides comprising third-order nonlinear and linear materials

Fuhao Liu [a], Wei Yang [b], Jichun Li [c,*]

[a] School of Mathematics and Computational Science, Xiangtan University, Xiangtan, 411105, Hunan, PR China
[b] Hunan Key Laboratory for Computation and Simulation in Science and Engineering, School of Mathematics and Computational Science, Xiangtan University, Xiangtan, 411105, Hunan, PR China
[c] Department of Mathematical Sciences, University of Nevada, Las Vegas, NV 89154-4020, USA

ARTICLE INFO

Article history:
Received 3 September 2022
Received in revised form 2 December 2022

Keywords:
Maxwell's equations
FETD methods
Photonic crystals
Nonlinear optics
Perfectly matched layers

ABSTRACT

In this paper, we design a time-domain finite element (FETD) algorithm for solving Maxwell's equations in third-order nonlinear media. The Cardano's method is used to solve the nonlinear constitutive equation. At the same time, we also establish the continuous stability of the third-order nonlinear model and the numerical stability of the FETD scheme. In order to reduce the wave reflection from the truncated domain boundary, the anisotropic perfectly matched layer model is developed and solved. Extensive numerical simulations are carried out and they demonstrate that bistable transmission switches depending on the incident wave's intensity can be obtained if a number of rods made of Kerr-type nonlinear materials are inserted around the bend of the linear bent photonic crystal waveguides.

1. Introduction

Metamaterials are a type of artificial nanomaterials obtained by combining different types of materials. This type of materials can control the effective permittivity and permeability and in the same time achieve some nice features required in many applications. Similar to metamaterials, photonic crystals (PCs) are artificial materials obtained by periodically arranging dielectrics with different permittivities. Since Yablonovitch [1] and John [2] respectively proposed the photonic band gap (PBG) structure (photonic crystals) in 1987, PCs have attracted the interest of many researchers (cf. monograph [3] and references cited therein), due to their PBG characteristics. The structural characteristics of PCs and metamaterials are very similar, and both of them are new artificial materials, but there are some differences between them [4,5]. Because diffraction phenomena should not occur in metamaterials, the unit cells that make up the metamaterials should be much smaller than the wavelength. Therefore, the effective permittivity and permeability of metamaterials can be obtained through the effective medium theory. PBG is the most important characteristic of PCs, and comes from the diffraction effect. This requires the unit cells of PCs to be close to the wavelength. Because of their periodic structures, the parameters of the materials comprising PCs will change periodically, and so will the refractive index inside the photonic crystal. Therefore, there are PBGs in PCs that are similar to electronic bands in semiconductor materials. PBG is a certain frequency range in which electromagnetic waves cannot pass through the photonic crystal. Due to this characteristic, PCs can be applied in many fields with good prospects. Some researchers change the local properties of PCs by inserting point defects or line defects inside PCs, and the line defects in PCs form a photonic crystal waveguide

* Corresponding author.
E-mail addresses: liufuhaoedu@163.com (F. Liu), yangwei@xtu.edu.cn (W. Yang), jichun.li@unlv.edu (J. Li).

https://doi.org/10.1016/j.cam.2022.115005
0377-0427/

(PCWG) [6,7]. Research [8] shows that the electromagnetic waves can pass through the sharp bends of PCWGs with high transmission efficiency.

Since the advent of PCs, there have been many efficient numerical methods developed to simulate the propagation of electromagnetic waves in PCs, such as finite-difference time-domain (FDTD) method [9], and finite element method (FEM) [10–13] etc. Currently, numerical simulations of wave propagation in PCs are mostly based on the FDTD method or commercial software [7] for frequency-domain simulation. While in practice, most of PCs are composed of nonrectangular cell units. Therefore, a numerical algorithm, such as FEM which has an advantage in handling complex geometries, is a better choice. Considering that researches based on the finite element time-domain (FETD) method for wave propagation in PCs are few, in this paper we propose and study an FETD method to simulate the propagation of electromagnetic waves in PCWGs.

Since the PBG of the photonic crystal is affected by the permittivity of the dielectric materials that compose the photonic crystal and the geometry (include arrangement and the sizes of lattices) of the photonic crystal, therefore, the change of the permittivity will affect the propagation of waves in the PCWG. The permittivity of the nonlinear material is related to the electric field. With this principle, we can insert several cells made of nonlinear dielectric material into linear PCWG to affect the transmission of electromagnetic waves. We only consider third-order nonlinear media. Kerr-type and Raman-type media are two relatively common third-order nonlinear media. The time-domain numerical methods for simulating Kerr media mainly include FDTD [9,14,15] and FETD methods [16–20]. At present, though there are many published papers on the FETD methods for Maxwell's equations in various media (e.g., [21–28]), there are relatively few articles using the FETD method to simulate PCs containing Kerr media and Raman media.

In this paper, we propose an FETD algorithm to solve the third-order nonlinear Maxwell's equations, and use the Cardano's method to solve the third-order nonlinear constitutive equation to avoid the iteration error and improve the efficiency of calculation. The numerical stability of the FETD scheme solving the Kerr-type nonlinear Maxwell's equations is proved. In addition, we apply the anisotropic perfect matched layer (APML) technology to our FETD algorithm to reduce the reflection at the boundary. In the numerical experiments, several bent nonlinear PCWGs have been designed by inserting nonlinear dielectric rods at the bend of the linear waveguides, which are based on square and triangular unit cells. The propagation of sine waves with different frequencies and intensities passing through the linear and nonlinear PCWGs are simulated. The Kerr-type nonlinear PCWG becomes a bistable transmission optical switch related to the wave's intensity.

The content of this paper is organized as follows. In Section 2, we develop the third-order nonlinear time-dependent Maxwell's equations, and prove the continuous stability of the Kerr–Maxwell's equations. In Section 3, we design a FETD scheme to solve the Maxwell's equations in the third-order nonlinear materials, and use a non-iterative the Cardano's method, to solve the nonlinear constitutive equation. The numerical stability of the FETD scheme of the Kerr–Maxwell's equations is also proved. In Section 4, we obtain the APML-FETD method by extending our FETD method to the anisotropic perfectly matched layer (APML) developed for the nonlinear Maxwell's equation. In the numerical experiments, several nonlinear PCWGs are designed, and we simulate the propagation of the sine waves in the nonlinear PCWGs by using our APML-FETD scheme. The results show that we can obtain a bistable transmission optical switch related to the wave's intensity by inserting several rods with the Kerr-type nonlinearity at the bend of the linear PCWGs.

2. The modeling equation and stability analysis

Let $\Omega \in \mathbb{R}^3$ be a bounded, simply connected domain with a connected boundary $\partial\Omega$ and unit outward normal $\boldsymbol{n}$. Let $\Omega_t = \Omega \times (0, T]$, where T is the end time. Consider the Maxwell's equations in non-magnetic and lossless media:

$$\partial_t \boldsymbol{D} = \nabla \times \boldsymbol{H}, \quad (\boldsymbol{x}, t) \in \Omega_t, \tag{1}$$

$$\partial_t \boldsymbol{H} = -\mu_0^{-1} \nabla \times \boldsymbol{E}, \quad (\boldsymbol{x}, t) \in \Omega_t, \tag{2}$$

where μ_0 denotes the permeability in vacuum, $\boldsymbol{E}$, $\boldsymbol{H}$ and $\boldsymbol{D}$ are the electric field, magnetic field and electric flux density, respectively. The constitutive relation between $\boldsymbol{D}$ and $\boldsymbol{E}$ is

$$\boldsymbol{D} = \varepsilon_1 \boldsymbol{E} + \boldsymbol{P}, \tag{3}$$

where $\varepsilon_1 = \varepsilon_0 \varepsilon_\infty$, ε_0 denotes the permittivity in vacuum, ε_∞ is a positive constant and denotes the relative permittivity at infinite frequency. In third-order nonlinear media, the relation between the induced polarization $\boldsymbol{P}$ and electric field $\boldsymbol{E}$ is

$$\boldsymbol{P} = \varepsilon_2 \cdot (g(t) * |\boldsymbol{E}|^2)\boldsymbol{E}, \tag{4}$$

where $\varepsilon_2 = \varepsilon_0 \chi^{(3)}$, the positive constant $\chi^{(3)}$ denotes the third-order nonlinear optical susceptibility [29], and the response function $g(t)$ is given by [14, Sec. C]:

$$g(t) = \alpha\delta(t) + (1 - \alpha) g_R(t), \quad \alpha \in [0, 1],$$

where

$$g_R(t) = \tilde{A} \exp(-t/\tau_2) \sin(t/\tau_1) u(t), \quad \tilde{A} = \frac{\tau_1^2 + \tau_2^2}{\tau_1 \tau_2^2}.$$

Here $u(t)$ denotes the unit step function, and τ_1 and τ_2 are some positive time constants.

Letting $G = G(\boldsymbol{x}, t) = g(t) * |\boldsymbol{E}|^2$, we can rewrite (4) as

$$\boldsymbol{P} = \varepsilon_2 \cdot (\alpha|\boldsymbol{E}|^2 + (1-\alpha)G)\boldsymbol{E}. \tag{5}$$

When $\alpha = 0$ (only Raman-type nonlinearity), by using Fourier-transform, we can show that G satisfies the constitutive equation (cf. [14, Sec. C])

$$a_1\partial_{tt}G + a_2\partial_t G + a_3 G = |\boldsymbol{E}|^2, \tag{6}$$

where constants $a_1 = \frac{\tau_1}{\tilde{A}}, a_2 = \frac{2\tau_1}{\tilde{A}\tau_2}, a_3 = 1$. When $\alpha = 1$ (a Kerr-type medium), we have $g(t) = \delta(t)$, which leads to $G = |\boldsymbol{E}|^2$. This can still be written in the form of (6) with $a_1 = a_2 = 0$ and $a_3 = 1$.

Therefore, substituting Eqs. (3) and (5) into Eq. (1), we obtain the time-domain Maxwell's equations in the third-order nonlinear material written as

$$\varepsilon_1\partial_t\boldsymbol{E} + \varepsilon_2 \cdot (\alpha\partial_t(|\boldsymbol{E}|^2\boldsymbol{E}) + (1-\alpha)\partial_t(G\boldsymbol{E})) - \nabla\times\boldsymbol{H} = 0, \tag{7}$$

$$\mu_0\partial_t\boldsymbol{H} + \nabla\times\boldsymbol{E} = 0, \tag{8}$$

$$a_1\partial_{tt}G + a_2\partial_t G + a_3 G = |\boldsymbol{E}|^2, \tag{9}$$

for any $(\boldsymbol{x}, t) \in \Omega_t$.

To complete the model (7)–(9), we assume that a perfect magnetic conductor (PMC) boundary condition is imposed on $\partial\Omega$:

$$\boldsymbol{n}\times\boldsymbol{H} = 0, \quad \text{on} \quad \partial\Omega\times(0,T], \tag{10}$$

where $\boldsymbol{n}$ denotes the unit outward normal on $\partial\Omega$. In addition, the initial conditions are

$$\begin{aligned} &\boldsymbol{E}(\boldsymbol{x};0) = \boldsymbol{E}^0(\boldsymbol{x}), \quad \boldsymbol{H}(\boldsymbol{x};0) = \boldsymbol{H}^0(\boldsymbol{x}),\\ &G(\boldsymbol{x},0) = G^0(\boldsymbol{x}), \quad \partial_t G(\boldsymbol{x},0) = G_1^0(\boldsymbol{x}), \quad \forall\boldsymbol{x}\in\Omega, \end{aligned} \tag{11}$$

where $\boldsymbol{E}^0(\boldsymbol{x})$, $\boldsymbol{H}^0(\boldsymbol{x})$, $G^0(\boldsymbol{x})$ and $G_1^0(\boldsymbol{x})$ are some given proper functions.

Assuming the existence of a sufficiently smooth solution to (7)–(11), a weak formulation can be obtained as follows. Multiplying (7)–(9) by $\boldsymbol{\varphi} \in (L^2(\Omega))^3$, $\boldsymbol{\psi} \in H_0(curl;\Omega)$ and $\phi \in L^2(\Omega)$, respectively, and integrating the results over Ω, then using the vector form of Green's theorem and PMC boundary condition (10), we can obtain the weak formulation of problem (7)–(11) as follows: Find the solution $(\boldsymbol{E}, \boldsymbol{H}, G)$ satisfies

$$(\varepsilon_1\partial_t\boldsymbol{E} + \varepsilon_2\alpha\partial_t(|\boldsymbol{E}|^2\boldsymbol{E}) + \varepsilon_2(1-\alpha)\partial_t(G\boldsymbol{E}), \boldsymbol{\varphi}) = (\nabla\times\boldsymbol{H}, \boldsymbol{\varphi}), \quad \forall\boldsymbol{\varphi}\in(L^2(\Omega))^3, \tag{12}$$

$$(\mu_0\partial_t\boldsymbol{H}, \boldsymbol{\psi}) = -(\nabla\times\boldsymbol{\psi}, \boldsymbol{E}), \quad \forall\boldsymbol{\psi}\in H_0(curl;\Omega), \tag{13}$$

$$(a_1\partial_{tt}G + a_2\partial_t G + a_3 G, \phi) = (|\boldsymbol{E}|^2, \phi), \quad \forall\phi\in L^2(\Omega), \tag{14}$$

for any $t \in (0, T]$ subject to the initial conditions (11).

In the rest of the paper, we denote the L^2 norm $\|\boldsymbol{u}\|_0^2 = \int_\Omega |\boldsymbol{u}|^2 d\Omega$.

Theorem 2.1. *Let*

$$\begin{aligned} &\boldsymbol{E} \in C^1(0,T;(L^2(\Omega))^3) \cap C(0,T;(L^4(\Omega))^3),\\ &\boldsymbol{H} \in C^1(0,T;(L^2(\Omega))^3) \cap C(0,T;H_0(curl;\Omega)),\\ &G \in C^2(0,T;L^2(\Omega)), \end{aligned} \tag{15}$$

satisfy (12)–(14), (10) and (11), *and* $G(\mathbf{x}, t) \geq 0$ *on* $\overline{\Omega}_t$. *Then* $(\boldsymbol{E}, \boldsymbol{H}, G)$ *satisfies the energy identity:*

$$\begin{aligned} &\frac{d}{dt}\left[\mu_0\|\boldsymbol{H}\|_0^2 + \varepsilon_1\|\boldsymbol{E}\|_0^2 + \frac{3\varepsilon_2\alpha}{2}\||\boldsymbol{E}|^2\|_0^2 + \varepsilon_2(1-\alpha)\left(\|G^{\frac{1}{2}}\boldsymbol{E}\|_0^2 + \frac{a_1}{2}\|\partial_t G\|_0^2 + \frac{a_3}{2}\|G\|_0^2\right)\right]\\ &+ \varepsilon_2(1-\alpha)a_2\|\partial_t G\|_0^2 = 0. \end{aligned}$$

and the stability

$$\begin{aligned} &\left[\mu_0\|\boldsymbol{H}\|_0^2 + \varepsilon_1\|\boldsymbol{E}\|_0^2 + \frac{3\varepsilon_2\alpha}{2}\||\boldsymbol{E}|^2\|_0^2 + \frac{\varepsilon_2(1-\alpha)}{2}(2\|G^{\frac{1}{2}}\boldsymbol{E}\|_0^2 + a_1\|\partial_t G\|_0^2 + a_3\|G\|_0^2)\right](t)\\ &\leqslant\left[\mu_0\|\boldsymbol{H}\|_0^2 + \varepsilon_1\|\boldsymbol{E}\|_0^2 + \frac{3\varepsilon_2\alpha}{2}\||\boldsymbol{E}|^2\|_0^2 + \frac{\varepsilon_2(1-\alpha)}{2}(2\|G^{\frac{1}{2}}\boldsymbol{E}\|_0^2 + a_1\|\partial_t G\|_0^2 + a_3\|G\|_0^2)\right](0), \end{aligned}$$

for any $t \in [0, T]$.

Proof. Taking $\boldsymbol{\psi} = \boldsymbol{H}, \boldsymbol{\varphi} = \boldsymbol{E}, \phi = \partial_t G(t)$ in (12)–(14), respectively, and adding (13) and (12) together, we obtain the following equations:

$$\varepsilon_1(\partial_t \boldsymbol{E}, \boldsymbol{E}) + \varepsilon_2\alpha(\partial_t(|\boldsymbol{E}|^2\boldsymbol{E}), \boldsymbol{E}) + \varepsilon_2(1-\alpha)(G\partial_t\boldsymbol{E} + (\partial_t G)\boldsymbol{E}, \boldsymbol{E}) + (\mu_0\partial_t\boldsymbol{H}, \boldsymbol{H}) = 0, \tag{16}$$

$$(a_1\partial_{tt}G + a_2\partial_t G + a_3 G, \partial_t G) = (|\boldsymbol{E}|^2, \partial_t G). \tag{17}$$

Substituting the following identities

$$\begin{aligned}(\partial_t(|\boldsymbol{E}|^2\boldsymbol{E}), \boldsymbol{E}) &= (\partial_t|\boldsymbol{E}|^2\boldsymbol{E} + |\boldsymbol{E}|^2\partial_t\boldsymbol{E}, \boldsymbol{E})\\ &= \int_\Omega |\boldsymbol{E}|^2\partial_t|\boldsymbol{E}|^2 d\Omega + \frac{1}{2}\int_\Omega |\boldsymbol{E}|^2\partial_t|\boldsymbol{E}|^2 d\Omega\\ &= \frac{3}{2}\int_\Omega |\boldsymbol{E}|^2\partial_t|\boldsymbol{E}|^2 d\Omega = \frac{3}{4}\frac{d}{dt}\|\,|\boldsymbol{E}|^2\|_0^2,\\ (G\partial_t\boldsymbol{E} + (\partial_t G)\boldsymbol{E}, \boldsymbol{E}) &= \frac{1}{2}\int_\Omega G\partial_t|\boldsymbol{E}|^2 d\Omega + \int_\Omega (\partial_t G)|\boldsymbol{E}|^2 d\Omega\\ &= \frac{1}{2}\left[\frac{d}{dt}\|G^{\frac{1}{2}}\boldsymbol{E}\|_0^2 + \int_\Omega (\partial_t G)|\boldsymbol{E}|^2 d\Omega\right],\end{aligned}$$

$$\varepsilon_1(\partial_t\boldsymbol{E}, \boldsymbol{E}) = \frac{\varepsilon_1}{2}\frac{d}{dt}\|\boldsymbol{E}\|_0^2,$$

$$(\mu_0\partial_t\boldsymbol{H}, \boldsymbol{H}) = \frac{\mu_0}{2}\frac{d}{dt}\|\boldsymbol{H}\|_0^2,$$

into (16), we have

$$\frac{d}{dt}\left(\mu_0\|\boldsymbol{H}\|_0^2 + \varepsilon_1\|\boldsymbol{E}\|_0^2 + \frac{3\varepsilon_2\alpha}{2}\|\,|\boldsymbol{E}|^2\|_0^2\right) + \varepsilon_2(1-\alpha)\left(\frac{d}{dt}\|G^{\frac{1}{2}}\boldsymbol{E}\|_0^2 + \int_\Omega (\partial_t G)|\boldsymbol{E}|^2 d\Omega\right) = 0. \tag{18}$$

From (17), we have

$$\begin{aligned}\int_\Omega (\partial_t G)|\boldsymbol{E}|^2 d\Omega &= \int_\Omega \partial_t G\,[a_1\partial_{tt}G + a_2\partial_t G + a_3 G]\,d\Omega\\ &= \frac{a_1}{2}\int_\Omega \partial_t(\partial_t G)^2 d\Omega + a_2\int_\Omega (\partial_t G)^2 d\Omega + \frac{a_3}{2}\int_\Omega \partial_t(G^2) d\Omega\\ &= \frac{a_1}{2}\frac{d}{dt}\|\partial_t G\|_0^2 + a_2\|\partial_t G\|_0^2 + \frac{a_3}{2}\frac{d}{dt}\|G\|_0^2.\end{aligned} \tag{19}$$

Therefore, substituting (19) into (18), we obtain

$$\begin{aligned}&\frac{d}{dt}\left(\mu_0\|\boldsymbol{H}\|_0^2 + \varepsilon_1\|\boldsymbol{E}\|_0^2 + \frac{3\varepsilon_2\alpha}{2}\|\,|\boldsymbol{E}|^2\|_0^2\right)\\ &+ \varepsilon_2(1-\alpha)\left[\frac{d}{dt}\|G^{\frac{1}{2}}\boldsymbol{E}\|_0^2 + \frac{a_1}{2}\frac{d}{dt}\|\partial_t G\|_0^2 + a_2\|\partial_t G\|_0^2 + \frac{a_3}{2}\frac{d}{dt}\|G\|_0^2\right] = 0.\end{aligned}$$

Furthermore, we have

$$\begin{aligned}&\frac{d}{dt}\left(\mu_0\|\boldsymbol{H}\|_0^2 + \varepsilon_1\|\boldsymbol{E}\|_0^2 + \frac{3\varepsilon_2\alpha}{2}\|\,|\boldsymbol{E}|^2\|_0^2 + \varepsilon_2(1-\alpha)(\|G^{\frac{1}{2}}\boldsymbol{E}\|_0^2 + \frac{a_1}{2}\|\partial_t G\|_0^2 + \frac{a_3}{2}\|G\|_0^2)\right)\\ &= -a_2\varepsilon_2(1-\alpha)\|\partial_t G\|_0^2 \leqslant 0.\end{aligned} \tag{20}$$

Integrating (20) with respect to t from $t = 0$ to any $t \in (0, T]$ completes our proof. □

3. The fully discrete schemes and their stability analysis

3.1. The three dimensional FETD scheme and its stability

We divide Ω into a number of tetrahedra whose maximum mesh size is h. Let T_h be the set of these tetrahedra. In any tetrahedron, we introduce two space as follows [30]:

$$R_1 = \{\boldsymbol{u} : \boldsymbol{u} = \boldsymbol{a} + \boldsymbol{b}\times\boldsymbol{x}, \boldsymbol{a}, \boldsymbol{b} \in \mathbb{R}^3\},$$

$$D_1 = \{\boldsymbol{u} : \boldsymbol{u} = \boldsymbol{a} + b\boldsymbol{x}, \boldsymbol{a} \in \mathbb{R}^3, b \in \mathbb{R}\}.$$

Consider the finite element spaces

$$\boldsymbol{V}_h = \{\boldsymbol{v}_h \in H(curl; \Omega) : \boldsymbol{v}_h|_e \in R_1, \forall e \in T_h\},$$

$$\boldsymbol{U}_h = \{\boldsymbol{u}_h \in (L^4(\Omega))^3 : \boldsymbol{u}_h|_e \in D_1, \forall e \in T_h\},$$
$$\boldsymbol{V}_h^0 = \{\boldsymbol{v}_h \in \boldsymbol{V}_h : \boldsymbol{v}_h \times \boldsymbol{n} = 0, \quad \text{on} \quad \partial\Omega\}.$$

In order to obtain the fully discrete FETD scheme, we divide the time interval [0,T] into N uniform subintervals $[(k-1)\tau, k\tau]$ by points $t_k = k\tau$, where the time step $\tau = \frac{T}{N}$, and $k = 0, 1, 2, \ldots, N$. We denote $\boldsymbol{E}_h^k$ for the approximate solution $\boldsymbol{E}$ at time t_k, and $\boldsymbol{H}_h^{k+\frac{1}{2}}$ for the approximate solution of $\boldsymbol{H}$ at time $t_{k+\frac{1}{2}}$.

First, we give several identities

$$\partial_t(|\boldsymbol{E}|^2) = \partial_t(E_x^2 + E_y^2 + E_z^2) = 2\boldsymbol{E}^\top \partial_t \boldsymbol{E},$$

$$\begin{aligned}\partial_t(|\boldsymbol{E}|^2\boldsymbol{E}) &= \partial_t(|\boldsymbol{E}|^2)\boldsymbol{E} + |\boldsymbol{E}|^2\partial_t\boldsymbol{E} = 2(\boldsymbol{E}^\top\partial_t\boldsymbol{E})\boldsymbol{E} + |\boldsymbol{E}|^2\partial_t\boldsymbol{E} \\ &= 2\boldsymbol{E}(\boldsymbol{E}^\top\partial_t\boldsymbol{E}) + |\boldsymbol{E}|^2\partial_t\boldsymbol{E} = 2(\boldsymbol{E}\boldsymbol{E}^\top)\partial_t\boldsymbol{E} + |\boldsymbol{E}|^2\partial_t\boldsymbol{E}.\end{aligned} \tag{21}$$

Using the following approximations

$$\boldsymbol{E}\boldsymbol{E}^\top|_{t=(k+\frac{1}{2})\tau} \approx \frac{\boldsymbol{E}^{k+1}(\boldsymbol{E}^{k+1})^\top + \boldsymbol{E}^k(\boldsymbol{E}^k)^\top}{2},$$
$$|\boldsymbol{E}|^2|_{t=(k+\frac{1}{2})\tau} \approx \frac{|\boldsymbol{E}^{k+1}|^2 + |\boldsymbol{E}^k|^2}{2},$$
$$\partial_t\boldsymbol{E}|_{t=(k+\frac{1}{2})\tau} \approx \frac{\boldsymbol{E}^{k+1} - \boldsymbol{E}^k}{\tau},$$

to discrete (21), we have

$$\partial_t(|\boldsymbol{E}|^2\boldsymbol{E})|_{t=(k+\frac{1}{2})\tau} \approx (\boldsymbol{E}^{k+1}(\boldsymbol{E}^{k+1})^\top + \boldsymbol{E}^k(\boldsymbol{E}^k)^\top)\frac{\boldsymbol{E}^{k+1} - \boldsymbol{E}^k}{\tau} + \frac{|\boldsymbol{E}^{k+1}|^2 + |\boldsymbol{E}^k|^2}{2}\frac{\boldsymbol{E}^{k+1} - \boldsymbol{E}^k}{\tau}. \tag{22}$$

Now we can develop a leap-frog type scheme to solve the weak formulation problem (12)–(14) and (11) with $\alpha = 1$. Given initial approximations $\boldsymbol{E}_h^0$, $\boldsymbol{H}_h^{\frac{1}{2}}$, for $k = 0, 1, 2, \ldots$, find $\boldsymbol{E}_h^{k+1} \in \boldsymbol{U}_h$, $\boldsymbol{H}_h^{k+\frac{3}{2}} \in \boldsymbol{V}_h^0$ such that

$$\begin{aligned}&\left(\varepsilon_2(\boldsymbol{E}_h^{k+1}(\boldsymbol{E}_h^{k+1})^\top + \boldsymbol{E}_h^k(\boldsymbol{E}_h^k)^\top)\frac{\boldsymbol{E}_h^{k+1} - \boldsymbol{E}_h^k}{\tau}, \boldsymbol{\varphi}_h\right) \\ &+ \left(\left(\varepsilon_1 + \varepsilon_2\frac{|\boldsymbol{E}_h^{k+1}|^2 + |\boldsymbol{E}_h^k|^2}{2}\right)\frac{\boldsymbol{E}_h^{k+1} - \boldsymbol{E}_h^k}{\tau}, \boldsymbol{\varphi}_h\right) = (\nabla \times \boldsymbol{H}_h^{k+\frac{1}{2}}, \boldsymbol{\varphi}_h),\end{aligned} \tag{23}$$

$$\left(\mu_0\frac{\boldsymbol{H}_h^{k+\frac{3}{2}} - \boldsymbol{H}_h^{k+\frac{1}{2}}}{\tau}, \boldsymbol{\psi}_h\right) = -(\boldsymbol{E}_h^{k+1}, \nabla \times \boldsymbol{\psi}_h), \tag{24}$$

hold true for any $\boldsymbol{\varphi}_h \in \boldsymbol{U}_h$ and $\boldsymbol{\psi}_h \in \boldsymbol{V}_h^0$.

Theorem 3.1. *Let $C_v = 1/\sqrt{\varepsilon_0\mu_0}$ be the speed of light in vacuum, and C_{inv} denotes the constant from the standard inverse estimate [31]*

$$\|\nabla \times \boldsymbol{\psi}_h\|_0 \leqslant C_{inv}h^{-1}\|\boldsymbol{\psi}_h\|_0, \forall \boldsymbol{\psi}_h \in \boldsymbol{V}_h. \tag{25}$$

Then under the time step constraint $\tau \leqslant \frac{h\sqrt{\varepsilon_\infty}}{C_{inv}C_v}$, the solutions of (23)–(24) satisfy the following stability:

$$\varepsilon_1\|\boldsymbol{E}_h^n\|_0^2 + \frac{3\varepsilon_2}{2}\|\,|\boldsymbol{E}_h^n|^2\|_0^2 + \mu_0\|\boldsymbol{H}_h^{n+\frac{1}{2}}\|_0^2 \leqslant 3\left(\varepsilon_1\|\boldsymbol{E}_h^0\|_0^2 + \frac{3\varepsilon_2}{2}\|\,|\boldsymbol{E}_h^0|^2\|_0^2 + \mu_0\|\boldsymbol{H}_h^{\frac{1}{2}}\|_0^2\right).$$

Proof. Choosing $\boldsymbol{\varphi}_h = \tau(\boldsymbol{E}_h^{k+1} + \boldsymbol{E}_h^k)$ in (23), $\boldsymbol{\psi}_h = \tau(\boldsymbol{H}_h^{k+\frac{3}{2}} + \boldsymbol{H}_h^{k+\frac{1}{2}})$ in (24), we can obtain the following:

$$\begin{aligned}&\varepsilon_2\left((\boldsymbol{E}_h^{k+1}(\boldsymbol{E}_h^{k+1})^\top + \boldsymbol{E}_h^k(\boldsymbol{E}_h^k)^\top)\tfrac{\boldsymbol{E}_h^{k+1} - \boldsymbol{E}_h^k}{\tau}, \tau(\boldsymbol{E}_h^{k+1} + \boldsymbol{E}_h^k)\right) \\ &+ \left(\left(\varepsilon_1 + \varepsilon_2\tfrac{|\boldsymbol{E}_h^{k+1}|^2 + |\boldsymbol{E}_h^k|^2}{2}\right)\tfrac{\boldsymbol{E}_h^{k+1} - \boldsymbol{E}_h^k}{\tau}, \tau(\boldsymbol{E}_h^{k+1} + \boldsymbol{E}_h^k)\right) = (\nabla \times \boldsymbol{H}_h^{k+\frac{1}{2}}, \tau(\boldsymbol{E}_h^{k+1} + \boldsymbol{E}_h^k)),\end{aligned} \tag{26}$$

$$\mu_0(\|\boldsymbol{H}_h^{k+\frac{3}{2}}\|_0^2 - \|\boldsymbol{H}_h^{k+\frac{1}{2}}\|_0^2) = -\tau(\boldsymbol{E}_h^{k+1}, \nabla \times (\boldsymbol{H}_h^{k+\frac{3}{2}} + \boldsymbol{H}_h^{k+\frac{1}{2}})). \tag{27}$$

Using the following identities

$$\begin{aligned}
&\left(\left(\boldsymbol{E}_h^{k+1}(\boldsymbol{E}_h^{k+1})^\top+\boldsymbol{E}_h^k(\boldsymbol{E}_h^k)^\top\right)\tfrac{\boldsymbol{E}_h^{k+1}-\boldsymbol{E}_h^k}{\tau},\ \tau(\boldsymbol{E}_h^{k+1}+\boldsymbol{E}_h^k)\right)\\
=\ &\left(\boldsymbol{E}_h^{k+1}(\boldsymbol{E}_h^{k+1})^\top\boldsymbol{E}_h^{k+1}-\boldsymbol{E}_h^k(\boldsymbol{E}_h^k)^\top\boldsymbol{E}_h^k\right.\\
&\left.+\ \boldsymbol{E}_h^k(\boldsymbol{E}_h^k)^\top\boldsymbol{E}_h^{k+1}-\boldsymbol{E}_h^{k+1}(\boldsymbol{E}_h^{k+1})^\top\boldsymbol{E}_h^k,\ \boldsymbol{E}_h^{k+1}+\boldsymbol{E}_h^k\right)\\
=\ &\left(|\boldsymbol{E}_h^{k+1}|^2\boldsymbol{E}_h^{k+1}-|\boldsymbol{E}_h^k|^2\boldsymbol{E}_h^k+(\boldsymbol{E}_h^k-\boldsymbol{E}_h^{k+1})(\boldsymbol{E}_h^{k+1})^\top\boldsymbol{E}_h^k,\ \boldsymbol{E}_h^{k+1}+\boldsymbol{E}_h^k\right)\\
=\ &\|\,|\boldsymbol{E}_h^{k+1}|^2\|_0^2-\|\,|\boldsymbol{E}_h^k|^2\|_0^2+\left((\boldsymbol{E}_h^{k+1})^\top\boldsymbol{E}_h^k,\ |\boldsymbol{E}_h^{k+1}|^2-|\boldsymbol{E}_h^k|^2\right)\\
&+\left((\boldsymbol{E}_h^{k+1})^\top\boldsymbol{E}_h^k,\ |\boldsymbol{E}_h^k|^2-|\boldsymbol{E}_h^{k+1}|^2\right)\\
=\ &\|\,|\boldsymbol{E}_h^{k+1}|^2\|_0^2-\|\,|\boldsymbol{E}_h^k|^2\|_0^2,\\
&\left(\tfrac{|\boldsymbol{E}_h^{k+1}|^2+|\boldsymbol{E}_h^k|^2}{2}\tfrac{\boldsymbol{E}_h^{k+1}-\boldsymbol{E}_h^k}{\tau},\ \tau(\boldsymbol{E}_h^{k+1}+\boldsymbol{E}_h^k)\right)=\tfrac{1}{2}\left(\|\,|\boldsymbol{E}_h^{k+1}|^2\|_0^2-\|\,|\boldsymbol{E}_h^k|^2\|_0^2\right),
\end{aligned}$$

we can rewrite (26) as

$$\varepsilon_1(\|\boldsymbol{E}_h^{k+1}\|_0^2-\|\boldsymbol{E}_h^k\|_0^2)+\frac{3\varepsilon_2}{2}(\|\,|\boldsymbol{E}_h^{k+1}|^2\|_0^2-\|\,|\boldsymbol{E}_h^k|^2\|_0^2)=\tau(\nabla\times\boldsymbol{H}_h^{k+\frac{1}{2}},\boldsymbol{E}_h^{k+1}+\boldsymbol{E}_h^k). \tag{28}$$

Adding Eqs. (27) and (28), and using the following identity

$$\begin{aligned}
&\tau(\nabla\times\boldsymbol{H}_h^{k+\frac{1}{2}},\boldsymbol{E}_h^{k+1}+\boldsymbol{E}_h^k)-\tau(\boldsymbol{E}_h^{k+1},\nabla\times(\boldsymbol{H}_h^{k+\frac{3}{2}}+\boldsymbol{H}_h^{k+\frac{1}{2}}))\\
=&\tau(\nabla\times\boldsymbol{H}_h^{k+\frac{1}{2}},\boldsymbol{E}_h^k)-\tau(\boldsymbol{E}_h^{k+1},\nabla\times\boldsymbol{H}_h^{k+\frac{3}{2}}),
\end{aligned}$$

we can obtain:

$$\begin{aligned}
\varepsilon_1(\|\boldsymbol{E}_h^{k+1}\|_0^2-\|\boldsymbol{E}_h^k\|_0^2)+\frac{3\varepsilon_2}{2}(\|\,|\boldsymbol{E}_h^{k+1}|^2\|_0^2-\|\,|\boldsymbol{E}_h^k|^2\|_0^2)+\mu_0(\|\boldsymbol{H}_h^{k+\frac{3}{2}}\|_0^2-\|\boldsymbol{H}_h^{n+\frac{1}{2}}\|_0^2)\\
=\tau(\nabla\times\boldsymbol{H}_h^{k+\frac{1}{2}},\boldsymbol{E}_h^k)-\tau(\boldsymbol{E}_h^{k+1},\nabla\times\boldsymbol{H}_h^{k+\frac{3}{2}}).
\end{aligned} \tag{29}$$

Summing (29) from $k=0$ to $k=n-1$, we obtain

$$\begin{aligned}
\varepsilon_1(\|\boldsymbol{E}_h^n\|_0^2-\|\boldsymbol{E}_h^0\|_0^2)+\frac{3\varepsilon_2}{2}(\|\,|\boldsymbol{E}_h^n|^2\|_0^2-\|\,|\boldsymbol{E}_h^0|^2\|_0^2)+\mu_0(\|\boldsymbol{H}_h^{n+\frac{1}{2}}\|_0^2-\|\boldsymbol{H}_h^{\frac{1}{2}}\|_0^2)\\
=\tau(\nabla\times\boldsymbol{H}_h^{\frac{1}{2}},\boldsymbol{E}_h^0)-\tau(\boldsymbol{E}_h^n,\nabla\times\boldsymbol{H}_h^{n+\frac{1}{2}}).
\end{aligned} \tag{30}$$

Using the Cauchy–Schwarz inequality and the standard inverse estimate (25), we have

$$\begin{aligned}
\tau(\boldsymbol{E}_h^n,\nabla\times\boldsymbol{H}_h^{n+\frac{1}{2}})&\leqslant\tau\cdot\|\boldsymbol{E}_h^n\|_0\cdot\|\nabla\times\boldsymbol{H}_h^{n+\frac{1}{2}}\|_0\\
&\leqslant\tau\cdot C_{inv}h^{-1}\|\boldsymbol{E}_h^n\|_0\cdot\|\boldsymbol{H}_h^{n+\frac{1}{2}}\|_0\\
&=\tau\cdot C_{inv}h^{-1}\cdot C_v\sqrt{\varepsilon_0}\|\boldsymbol{E}_h^n\|_0\cdot\sqrt{\mu_0}\|\boldsymbol{H}_h^{n+\frac{1}{2}}\|_0\\
&\leqslant\frac{\delta_1}{2}\varepsilon_0\|\boldsymbol{E}_h^n\|_0^2+\frac{1}{2\delta_1}\left(\tau C_{inv}h^{-1}C_v\right)^2\mu_0\|\boldsymbol{H}_h^{n+\frac{1}{2}}\|_0^2.
\end{aligned} \tag{31}$$

Letting $n=0$ in (31), we have

$$\tau(\boldsymbol{E}_h^0,\nabla\times\boldsymbol{H}_h^{\frac{1}{2}})\leqslant\frac{\delta_1}{2}\varepsilon_0\|\boldsymbol{E}_h^0\|_0^2+\frac{1}{2\delta_1}\left(\tau C_{inv}h^{-1}C_v\right)^2\mu_0\|\boldsymbol{H}_h^{\frac{1}{2}}\|_0^2. \tag{32}$$

Substituting (31) and (32) into (30), we obtain

$$\begin{aligned}
&\varepsilon_1(\|\boldsymbol{E}_h^n\|_0^2-\|\boldsymbol{E}_h^0\|_0^2)+\frac{3\varepsilon_2}{2}(\|\,|\boldsymbol{E}_h^n|^2\|_0^2-\|\,|\boldsymbol{E}_h^0|^2\|_0^2)+\mu_0(\|\boldsymbol{H}_h^{n+\frac{1}{2}}\|_0^2-\|\boldsymbol{H}_h^{\frac{1}{2}}\|_0^2)\\
\leqslant&\frac{\delta_1}{2}\varepsilon_0\|\boldsymbol{E}_h^n\|_0^2+\frac{1}{2\delta_1}\left(\tau C_{inv}h^{-1}C_v\right)^2\mu_0\|\boldsymbol{H}_h^{n+\frac{1}{2}}\|_0^2\\
&+\frac{\delta_1}{2}\varepsilon_0\|\boldsymbol{E}_h^0\|_0^2+\frac{1}{2\delta_1}\left(\tau C_{inv}h^{-1}C_v\right)^2\mu_0\|\boldsymbol{H}_h^{\frac{1}{2}}\|_0^2.
\end{aligned}$$

By choosing $\delta_1=\varepsilon_\infty$ and $\tau\leq\frac{h\sqrt{\varepsilon_\infty}}{C_{inv}C_v}$, we have

$$\varepsilon_1\|\boldsymbol{E}_h^n\|_0^2+\frac{3\varepsilon_2}{2}\|\,|\boldsymbol{E}_h^n|^2\|_0^2+\mu_0\|\boldsymbol{H}_h^{n+\frac{1}{2}}\|_0^2\leqslant 3\left(\varepsilon_1\|\boldsymbol{E}_h^0\|_0^2+\frac{3\varepsilon_2}{2}\|\,|\boldsymbol{E}_h^0|^2\|_0^2+3\mu_0\|\boldsymbol{H}_h^{\frac{1}{2}}\|_0^2\right),$$

which concludes the proof. □

3.2. The two dimensional FETD scheme

Next, we consider the two-dimensional form of problem (7)–(11). In this case, we assume that Ω is a bounded, simply connected domain in $\mathbb{R}^2$, and Ω is divided into a number of triangles with maximum mesh size h. Let T_h be the set of these triangles, and

$$\begin{aligned} \boldsymbol{H} &= [H_x, H_y]^\top, \qquad \nabla \times \boldsymbol{H} = \partial_x H_y - \partial_y H_x, \\ E &= E_z, \qquad \nabla \times E = [\partial_y E, -\partial_x E]^\top. \end{aligned}$$

We can directly write the two dimensional form of (12)–(14) as follows: Find the solution

$$\begin{aligned} &E \in C^1(0,T;L^2(\Omega)) \cap C(0,T;L^4(\Omega)), \\ &\boldsymbol{H} \in C^1(0,T;(L^2(\Omega))^2) \cap C(0,T;H_0(curl;\Omega)), \\ &G \in C^2(0,T;L^2(\Omega)), \end{aligned} \tag{33}$$

satisfies

$$(\varepsilon_1 \partial_t E + 3\varepsilon_2 \alpha |E|^2 \partial_t E + \varepsilon_2(1-\alpha)\partial_t(GE), \varphi) = (\nabla \times \boldsymbol{H}, \varphi), \qquad \forall \varphi \in L^2(\Omega), \tag{34}$$

$$(\mu_0 \partial_t \boldsymbol{H}, \boldsymbol{\psi}) = -(\nabla \times \boldsymbol{\psi}, E), \qquad \forall \boldsymbol{\psi} \in H_0(curl;\Omega), \tag{35}$$

$$(a_1 \partial_{tt} G + a_2 \partial_t G + a_3 G, \phi) = (|E|^2, \phi), \qquad \forall \phi \in L^2(\Omega), \tag{36}$$

for any $t \in (0, T]$ with the initial conditions (11).

Consider the finite element spaces

$$\begin{aligned} U_h &= \{v_h \in L^4(\Omega) : v_h|_e \text{ is a piecewise constant}, e \in T_h\}, \\ V_h &= \{\boldsymbol{v}_h \in H(curl;\Omega) : \boldsymbol{v}_h|_e = \text{span}\{\lambda_i \nabla \lambda_j - \lambda_j \nabla \lambda_i\}, i, j = 1, 2, 3, e \in T_h\}, \end{aligned}$$

where λ_i denotes the standard linear Lagrange basis function at vertex i of triangle e.

To approximate the weak formulation (34)–(36) with initial conditions (11), we propose the following fully discrete scheme: Given proper initial approximations $\boldsymbol{H}_h^{\frac{1}{2}}$, E_h^0 and E_h^{-1}, for $k = 0, 1, \ldots$, find $E_h^{k+1}, G_h^{k+1} \in U_h$, $\boldsymbol{H}_h^{k+\frac{3}{2}} \in V_h^0$ such that

$$\begin{aligned} &\left(\left(\varepsilon_1 + \tfrac{3\varepsilon_2\alpha}{2} \left(|E_h^{k+1}|^2 + |E_h^k|^2 \right) \right) \tfrac{E_h^{k+1} - E_h^k}{\tau}, \varphi_h \right) \\ &+ \left(\varepsilon_2(1-\alpha) \tfrac{G_h^{k+1} E_h^{k+1} - G_h^k E_h^k}{\tau}, \varphi_h \right) = (\nabla \times \boldsymbol{H}_h^{k+\frac{1}{2}}, \varphi_h), \end{aligned} \tag{37}$$

$$\left(\mu_0 \frac{\boldsymbol{H}_h^{k+\frac{3}{2}} - \boldsymbol{H}_h^{k+\frac{1}{2}}}{\tau}, \boldsymbol{\psi}_h \right) = -(E_h^{k+1}, \nabla \times \boldsymbol{\psi}_h), \tag{38}$$

$$\left(a_1 \frac{G_h^{k+1} - 2G_h^k + G_h^{k-1}}{\tau^2} + a_2 \frac{G_h^{k+1} - G_h^{k-1}}{2\tau} + a_3 G_h^k, \phi_h \right) = (|E_h^k|^2, \phi_h), \tag{39}$$

hold true for any $\varphi_h, \phi_h \in U_h$ and $\boldsymbol{\psi}_h \in V_h^0$.

The initial conditions (11) are discretized as follows:

$$\begin{aligned} E_h^0 = \Pi_2 E^0(\boldsymbol{x}), \ G_h^0 = \Pi_2 G^0(\boldsymbol{x}), \ \frac{G_h^1 - G_h^{-1}}{2\tau} = \Pi_2 G_1^0(\boldsymbol{x}), \\ \boldsymbol{H}_h^{\frac{1}{2}} = \Pi_c(\boldsymbol{H}^0(\boldsymbol{x}) + \frac{\tau}{2}\partial_t \boldsymbol{H}^0(\boldsymbol{x})) = \Pi_c(\boldsymbol{H}^0(\boldsymbol{x}) - \frac{\tau}{2}\mu_0^{-1} \nabla \times E^0(\boldsymbol{x})), \end{aligned} \tag{40}$$

where we used the governing Eqs. (8) in the last step. Here Π_2 denotes the standard L^2 projection to space U_h, and Π_c denotes the standard Nédélec interpolation [31] to space V_h.

The implementation of the scheme (37)–(39) is quite simple. At each time step, we first solve (39) for G_h^{k+1}; then solve (37) for E_h^{k+1}; finally, solve (38) for $\boldsymbol{H}_h^{k+\frac{1}{2}}$. When $k = 0$, we need to use the initial approximation to solve for G_h^1. More specifically, from (40) we have

$$G_h^{-1} = G_h^1 - 2\tau \Pi_2 G_1^0,$$

then substituting this into (39) with $k = 0$, we obtain

$$G_h^1 = \frac{1}{2a_1} \left[(2a_1 - \tau^2 a_3) G_h^0 + 2\tau(a_1 - 0.5\tau a_2) \Pi_2 G_1^0 + \tau^2 |E_h^0|^2 \right].$$

Note that Eq. (37) is equivalent to

$$\left(\varepsilon_1+\frac{3\varepsilon_2\alpha}{2}(|E_h^{k+1}|^2+|E_h^k|^2)\right)(E_h^{k+1}-E_h^k)+\varepsilon_2(1-\alpha)(G_h^{k+1}E_h^{k+1}-G_h^kE_h^k)=\tau\nabla\times\boldsymbol{H}_h^{k+\frac{1}{2}}, \tag{41}$$

in any element $e\in T_h$, which can be written as a third order polynomial equation as follows:

$$b_1z^3+b_2z^2+b_3z+b_4=0,\quad \text{with } z=E_h^{k+1} \tag{42}$$

where $b_1=\frac{3\varepsilon_2\alpha}{2}$, $b_2=-\frac{3\varepsilon_2\alpha}{2}E_h^k$, $b_3=\varepsilon_1+\frac{3\varepsilon_2\alpha}{2}(E_h^k)^2+\varepsilon_2(1-\alpha)G_h^{k+1}$ and $b_4=\tau\nabla\times\boldsymbol{H}_h^{k+\frac{1}{2}}+\varepsilon_1E_h^k+\frac{3\varepsilon_2\alpha}{2}(E_h^k)^3+\varepsilon_2(1-\alpha)G_h^kE_h^k$.

To avoid the computational cost by using the standard iterative method to solve (42), we introduce the Cardano's method to solve it with an exact formula. Assuming $b_1\neq 0$, let $z=y-\frac{b_2}{3b_1}$, $p=\frac{3b_1b_3-b_2^2}{3b_1^2}$, $q=\frac{27b_1^2b_4-9b_1b_2b_3+2b_2^3}{27b_1^3}$, Eq. (42) becomes as

$$y^3+py+q=0.$$

Let $\omega=\frac{-1+\sqrt{3}i}{2}$ and $\Delta=(\frac{q}{2})^2+(\frac{p}{3})^3$. If $\Delta\geqslant 0$, then the solutions y_1,y_2,y_3 of Eq. (42) are

$$\begin{aligned} y_1&=\sqrt[3]{-\frac{q}{2}+\sqrt{\Delta}}+\sqrt[3]{-\frac{q}{2}-\sqrt{\Delta}},\\ y_2&=\omega\sqrt[3]{-\frac{q}{2}+\sqrt{\Delta}}+\omega^2\sqrt[3]{-\frac{q}{2}-\sqrt{\Delta}},\\ y_3&=\omega^2\sqrt[3]{-\frac{q}{2}+\sqrt{\Delta}}+\omega\sqrt[3]{-\frac{q}{2}-\sqrt{\Delta}}. \end{aligned} \tag{43}$$

Under the assumption that $G(\cdot,t)$ is nonnegative on $\overline{\Omega}_t$ and our discrete scheme (37)–(39) is convergent (i.e., $|G_h^{k+1}-G(\mathbf{x},t_{k+1})|_{L^\infty(\Omega)}\leq C\tau^\delta$ for any $\delta>0$), we have

$$\begin{aligned} 3b_1b_3-b_2^2&=3\frac{3\varepsilon_2\alpha}{2}(\varepsilon_1+\frac{3\varepsilon_2\alpha}{2}(E_h^k)^2+\varepsilon_2(1-\alpha)G_h^{k+1})-(\frac{3\varepsilon_2\alpha}{2}E_h^k)^2\\ &=2(\frac{3\varepsilon_2\alpha}{2}E_h^k)^2+\frac{9\varepsilon_1\varepsilon_2\alpha}{2}+\frac{9\varepsilon_2^2\alpha(1-\alpha)}{2}G_h^{k+1}\geqslant 0, \end{aligned} \tag{44}$$

for sufficiently small τ. In this case, the unique real solution of (42) is $y_1-\frac{b_2}{3b_1}$, i.e., in our implementation, we simply choose $E_h^{k+1}=y_1-\frac{b_2}{3b_1}$ as the solution of (42) to avoid the computational cost of an iterative method.

4. 2-D FETD scheme based on APML

In the rest of the paper, we focus on 2-D simulation. To simulate the propagation of electromagnetic waves in a bounded domain, we choose the perfectly matched layer (PML) idea introduced by Berenger in 1994 [32]. Due to its effectiveness in absorbing outgoing waves, various PMLs have been developed and applied to solve various wave propagation problems (cf., [33–36] and references therein).

The anisotropic perfect matched layer (APML) was proposed by Gedney [37] for the FDTD method, and later was adopted by Fujii and Russer [14] to solve Maxwell's equations in 2-D Kerr–Raman-type nonlinear dispersive media. Due to its proved effectiveness in solving nonlinear Maxwell's equations, in this paper we will choose the APML method for our simulation.

First, let us develop the APML modeling equations. Consider the 3-D frequency-domain Maxwell's equations

$$\nabla\times\boldsymbol{\mathcal{H}}=j\omega\boldsymbol{\Lambda}\boldsymbol{\mathcal{D}}, \tag{45}$$

$$\nabla\times\boldsymbol{\mathcal{E}}=-j\omega\boldsymbol{\Lambda}\boldsymbol{\mathcal{B}}, \tag{46}$$

where $\boldsymbol{\mathcal{E}}$, $\boldsymbol{\mathcal{D}}$, $\boldsymbol{\mathcal{H}}$ and $\boldsymbol{\mathcal{B}}$ are the frequency-domain forms of $\boldsymbol{E}$, $\boldsymbol{D}$, $\boldsymbol{H}$ and magnetic flux density $\boldsymbol{B}$, respectively, $j=\sqrt{-1}$, and ω is the wave frequency. Here the uniaxial anisotropic medium tensor $\boldsymbol{\Lambda}$ is given as:

$$\boldsymbol{\Lambda}=\begin{bmatrix}\frac{s_ys_z}{s_x}&0&0\\0&\frac{s_xs_z}{s_y}&0\\0&0&\frac{s_xs_y}{s_z}\end{bmatrix},$$

with

$$s_x=\kappa_x+\frac{\sigma_x}{j\omega\varepsilon_0},\quad s_y=\kappa_y+\frac{\sigma_y}{j\omega\varepsilon_0},\quad s_z=\kappa_z+\frac{\sigma_z}{j\omega\varepsilon_0},$$

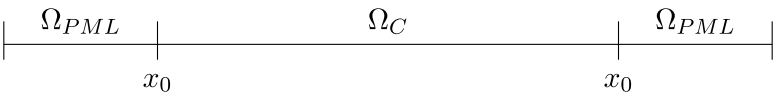

Fig. 1. The configuration of 1-D PML.

where $\kappa_x, \kappa_y, \kappa_z$ are the piecewise polynomial functions of x, y and z, respectively, and $\sigma_x, \sigma_y, \sigma_z$ are the damping functions in the x-, y- and z-directions, respectively. Usually, we choose $\kappa_i, \sigma_i, (i = x, y, z)$ as piecewise polynomial functions [15,32,37]. Taking κ_x, σ_x as an example, we choose

$$\kappa_x(x) = \begin{cases} 1 + (\kappa_x^{max} - 1)\left(\frac{|x-x_0|}{d}\right)^m, & x \in \Omega_{PML}, \\ 1, & x \in \Omega_C, \end{cases}$$

$$\sigma_x(x) = \begin{cases} \sigma_x^{max}\left(\frac{|x-x_0|}{d}\right)^m, & x \in \Omega_{PML}, \\ 0, & x \in \Omega_C, \end{cases}$$

where $|x - x_0|$ denotes the distance between x and x_0, constants κ_x^{max} and σ_x^{max} satisfy $\kappa_x^{max} \geqslant 1$ and $\sigma_x^{max} \geqslant 0$, respectively, and d denotes the thickness of the PML. According to [31], to reach a reflection error goal $R(0)$, we choose $\sigma_x^{max} = -\frac{(m+1)\varepsilon_0 C_v}{2d}\ln(R(0))$. A sketch of the configuration of PML surrounding the original physical domain is shown in Fig. 1.

Now we apply this APML method to the 2-D transverse magnetic model of (7)–(9). In this case, we have $s_z = \kappa_z = 1$, $H_z = E_x = E_y = 0$, and $\boldsymbol{\Lambda}$ becomes as

$$\boldsymbol{\Lambda} = \begin{bmatrix} \frac{s_y}{s_x} & 0 & 0 \\ 0 & \frac{s_x}{s_y} & 0 \\ 0 & 0 & s_x s_y \end{bmatrix}. \tag{47}$$

Substituting (47) into (45)–(46), we have

$$\nabla \times \boldsymbol{\mathcal{H}} = j\omega s_x s_y \mathcal{F}[\varepsilon_1 E + \alpha\varepsilon_2 E^3 + \varepsilon_2(1-\alpha)GE], \tag{48}$$

$$\nabla \times \mathcal{E} = -j\omega\mu_0 \begin{bmatrix} \frac{s_y}{s_x} & \\ & \frac{s_x}{s_y} \end{bmatrix} \boldsymbol{\mathcal{H}}, \tag{49}$$

where $\mathcal{F}[\cdot]$ denotes the Fourier transform.

Denoting

$$\mathcal{D} = s_y \mathcal{F}[\varepsilon_1 E + \alpha\varepsilon_2 E^3 + \varepsilon_2(1-\alpha)GE], \tag{50}$$

$$\boldsymbol{\mathcal{B}} = \mu_0(\boldsymbol{K}_1 + (j\omega\varepsilon_0)^{-1}\boldsymbol{Q}_1)^{-1}\boldsymbol{\mathcal{H}}, \tag{51}$$

we can rewrite Eqs. (48)–(49) as

$$\nabla \times \boldsymbol{\mathcal{H}} = j\omega s_x \mathcal{D}, \tag{52}$$

$$\nabla \times \mathcal{E} = -j\omega(\boldsymbol{K}_2 + (j\omega\varepsilon_0)^{-1}\boldsymbol{Q}_2)\boldsymbol{\mathcal{B}}, \tag{53}$$

where $\boldsymbol{K}_1 = diag(\kappa_x, \kappa_y)$, $\boldsymbol{K}_2 = diag(\kappa_y, \kappa_x)$, $\boldsymbol{Q}_1 = diag(\sigma_x, \sigma_y)$, and $\boldsymbol{Q}_2 = diag(\sigma_y, \sigma_x)$.

Applying the inverse Fourier transform to Eqs. (50)–(53), we obtain the coupled Maxwell's equations in the third-order nonlinear materials with its corresponding PML given as follows:

$$\begin{aligned} \kappa_x \partial_t D + \varepsilon_0^{-1}\sigma_x D &= \nabla \times \boldsymbol{H}, \\ \partial_t D = (\kappa_y \partial_t + \varepsilon_0^{-1}\sigma_y)[\varepsilon_1 E + \alpha\varepsilon_2 E^3 + \varepsilon_2(1-\alpha)GE], \\ \boldsymbol{K}_2 \partial_t \boldsymbol{B} + \varepsilon_0^{-1}\boldsymbol{Q}_2 \boldsymbol{B} &= -\nabla \times E, \\ \boldsymbol{K}_1 \partial_t \boldsymbol{B} + \varepsilon_0^{-1}\boldsymbol{Q}_1 \boldsymbol{B} &= \mu_0 \partial_t \boldsymbol{H}. \end{aligned}$$

The relation between G and E is the same as defined by Eq. (9).

Now we can present our APML-FETD scheme: Given proper initial approximations E_h^0, $\boldsymbol{H}_h^{-\frac{1}{2}}$, D_h^0, $\boldsymbol{B}_h^{-\frac{1}{2}}$, G_h^0, G_h^{-1}, find $E_h^{k+1}, D_h^{k+1}, G_h^{k+1} \in U_h$, $\boldsymbol{H}_h^{k+\frac{1}{2}}, \boldsymbol{B}_h^{k+\frac{1}{2}} \in V_h^0$ for any $k = 0, 1, \ldots$, such that

$$\left(\kappa_x \frac{D_h^{k+1} - D_h^k}{\tau}, \varphi_{1h}\right) + \left(\frac{\sigma_x}{\varepsilon_0}\frac{D_h^{k+1} + D_h^k}{2}, \varphi_{1h}\right) = \left(\nabla \times \boldsymbol{H}_h^{k+\frac{1}{2}}, \varphi_{1h}\right), \tag{54}$$

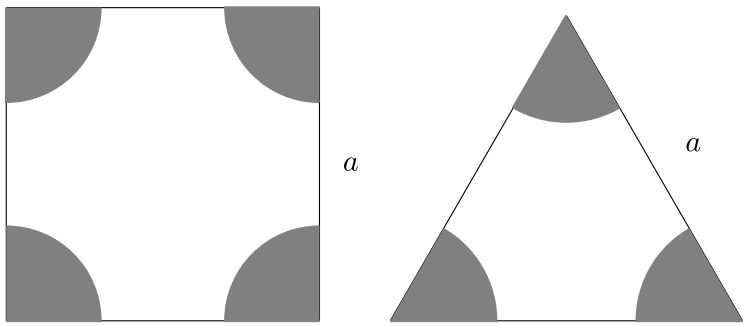

Fig. 2. Square and triangular unit cells. The background material (blank) is air; the gray sectors are dielectric rods.

$$\left(\left(\frac{a_1}{\tau^2}+\frac{a_2}{2\tau}\right)G_h^{k+1}+\left(a_3-\frac{2a_1}{\tau^2}\right)G_h^{k}+\left(\frac{a_1}{\tau^2}-\frac{a_2}{2\tau}\right)G_h^{k-1},\varphi_{2h}\right)=\left(|E_h^k|^2,\varphi_{2h}\right), \tag{55}$$

$$\begin{aligned}&\left(\frac{D_h^{k+1}-D_h^k}{\tau},\varphi_{3h}\right)=\varepsilon_1\left(\kappa_y\frac{E_h^{k+1}-E_h^k}{\tau}+\frac{\sigma_y}{\varepsilon_0}\frac{E_h^{k+1}+E_h^k}{2},\varphi_{3h}\right)\\&+\varepsilon_2\alpha\left(3\kappa_y\frac{(E_h^{k+1})^2+(E_h^k)^2}{2}\frac{E_h^{k+1}-E_h^k}{\tau}+\frac{\sigma_y}{\varepsilon_0}\frac{(E_h^{k+1})^3+(E_h^k)^3}{2},\varphi_{3h}\right)\\&+\varepsilon_2(1-\alpha)\left(\kappa_y\frac{G_h^{k+1}E_h^{k+1}-G_h^kE_h^k}{\tau}+\frac{\sigma_y}{\varepsilon_0}\frac{G_h^{k+1}E_h^{k+1}+G_h^kE_h^k}{2},\varphi_{3h}\right),\end{aligned} \tag{56}$$

$$\left(\boldsymbol{K}_2\frac{\boldsymbol{B}_h^{k+\frac12}-\boldsymbol{B}_h^{k-\frac12}}{\tau},\boldsymbol{\psi}_{1h}\right)+\left(\boldsymbol{Q}_2\frac{\boldsymbol{B}_h^{k+\frac12}+\boldsymbol{B}_h^{k-\frac12}}{2\varepsilon_0},\boldsymbol{\psi}_{1h}\right)=-(E_h^k,\nabla\times\boldsymbol{\psi}_{1h}), \tag{57}$$

$$\left(\mu_0\frac{\boldsymbol{H}_h^{k+\frac12}-\boldsymbol{H}_h^{k-\frac12}}{\tau},\boldsymbol{\psi}_{2h}\right)=\left(\boldsymbol{K}_1\frac{\boldsymbol{B}_h^{k+\frac12}-\boldsymbol{B}_h^{k-\frac12}}{\tau},\boldsymbol{\psi}_{2h}\right)+\left(\boldsymbol{Q}_1\frac{\boldsymbol{B}_h^{k+\frac12}+\boldsymbol{B}_h^{k-\frac12}}{2\varepsilon_0},\boldsymbol{\psi}_{2h}\right), \tag{58}$$

hold true for any $\varphi_{1h},\varphi_{2h},\varphi_{3h}\in U_h$ and $\boldsymbol{\psi}_{1h},\boldsymbol{\psi}_{2h}\in V_h^0$.

At each step, the APML-FETD algorithm is implemented as follows:

Step 1. Excite the source wave at the electric field, and use (57) to solve for $\boldsymbol{B}_h^{k+\frac12}$. When $k=0$, we need to couple (57) with an initial approximation $\frac{\boldsymbol{B}_h^{\frac12}+\boldsymbol{B}_h^{-\frac12}}{2}=\Pi_c\boldsymbol{B}(\mathbf{x},0)$ to obtain $\boldsymbol{B}_h^{\frac12}$;

Step 2. Use (58) to solve for $\boldsymbol{H}_h^{k+\frac12}$;

Step 3. Use (54) to solve for D_h^{k+1};

Step 4. Use (55) to update G_h^{k+1};

Step 5. Use (56) to obtain the coefficients b_1,b_2,b_3 and b_4 of the cubic Eq. (42), and substitute them into (43) to obtain E_h^{k+1}. Then go back to **Step 1** and repeat **Steps 1-5**.

5. Numerical results

In this section, we present our numerical simulations of wave propagation in photonic crystal waveguides formed by arranging triangular and square unit cells periodically (See Fig. 2). We are interested in those nonlinear PCWGs with some nonlinear dielectric rods inserted around the bends.

First, we set some conventions in the numerical experiments in this section. Figs. 3(a), 5(a), 7(a), 8(a), 9(a) and 10(a) are the sketches of our model setups. Taking Fig. 3(a) as an example, the most outside empty region between two rectangles is the PML region (having 10 mesh size thickness), the interested physical domain is surrounded by the PML, and has dimensions $[0,14a]\times[0,8a]$, where a denotes the lattice constant and is equal to 1 μm, the green rods always denote the linear dielectric materials with relative permittivity 11.56, the blank region between rods is air, the red arrow denotes the

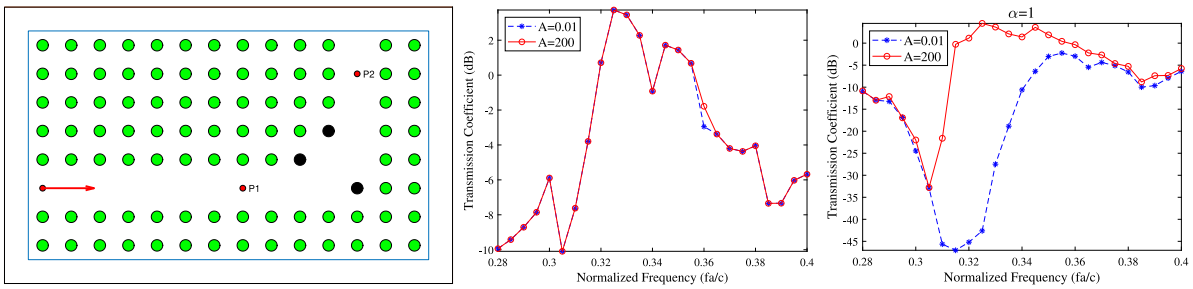

Fig. 3. Subfigure (1) is a L-shaped PCWG. In this experiment, we take $A = 0.01$ V/m, 200 V/m and frequencies in the range $[0.28c/a, 0.4c/a]$, where c is the speed of light in vacuum. Setting the black rods in Subfigure (1) as linear material rods and Kerr-type nonlinear material rods, the obtained corresponding transmission coefficients are shown in Subfigures (2) and (3), respectively.

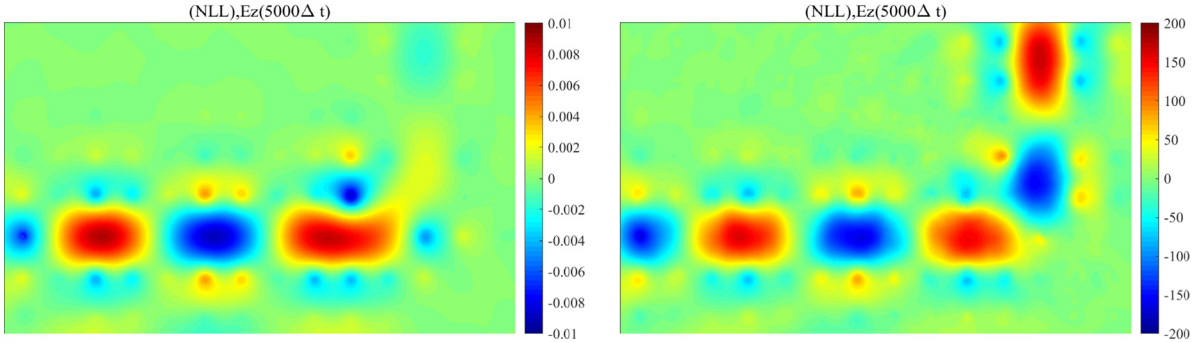

Fig. 4. The electric fields E_z obtained at time $t = 5000\Delta t$ for the Kerr-type nonlinear bent PCWG given in Fig. 3(a). The incoming waves are sine waves whose frequencies are $0.33c/a$, and intensities are 0.01 V/m (left) and 200 V/m (right), respectively. In this experiment, we consider the triangle mesh, whose mesh size is $h = \frac{a}{12}$, and the time step size $\tau = \frac{h}{6c}$.

position and direction of incident waves, and points P_1 and P_2 denote the two observation points. If we do not emphasize, the black rods represent the nonlinear materials such as the Kerr-type or Raman-type. In all our simulations, we fix the parameter ε_∞ of nonlinear material rods to be 7, the third-order nonlinear optical susceptibility $\chi^{(3)} = 0.001$, and the radius of the material rods $R = 0.2a$. We take sine wave $A\sin(2\pi ft)$ as the incident wave imposed as E_z, where f is the wave frequency, and A is the magnitude of the wave.

To make the expression more lucid, we define the transmission coefficient TC as $20\ln(\frac{\max|E_{P_2}|}{\max|E_{P_1}|})$, where E_{P_1} and E_{P_2} denote electric fields at P_1 and P_2, respectively. If the value of the parameter α is not marked, it means that the corresponding result is about the transmission coefficient in a bent linear waveguide. Since in the experiments of this paper, the inside of PML is the background material (air), here we can take $\kappa^{max} = 1$.

Below we will discuss the phenomena of wave passing through both linear and nonlinear bent PCWG comprised of triangular and square unit cells.

5.1. Kerr-type nonlinear bent PCWG

First, we imitate the design of the bent waveguide given in [9], and plot our first nonlinear bend waveguide (See Fig. 3(a)).

From Figs. 3(b), 5(b) and 7(b), it can be seen that low-intensity and high-intensity sine waves with different frequencies can pass through the bent linear PCWG well. The transmission coefficients are almost unaffected by the intensities of the waves. From Figs. 3(c), 5(c) and 7(c), it can be observed that the intensities and frequencies of the incident waves affect the transmission coefficients when the incident waves pass through the bent Kerr-type nonlinear PCWG. In certain frequency range (bistable frequency band), the transmission coefficients of high-intensity electromagnetic waves (The amplitudes of electric fields are 200 V/m) are larger than that of low-intensity electromagnetic waves. When different intensity incoming waves with frequency $f = 0.33c/a$ pass throuth the waveguides shown in Fig. 3(a) and Fig.5(a), we obtain the electric fields E_z shown in Figs. 4 and 6, respectively. Therefore, we can conclude that the high-intensity electromagnetic waves

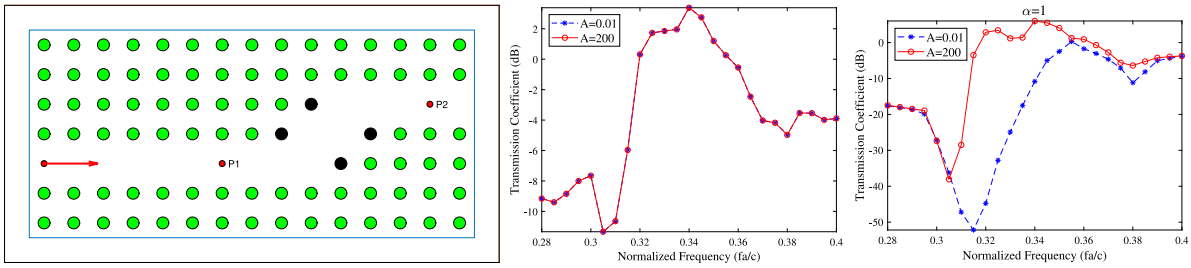

Fig. 5. Subfigure (1) is a Z-shaped PCWG. In this experiment, we use the same incident waves as the experiments in Fig. 3. Setting the black rods in Subfigure (1) as linear material rods and Kerr-type nonlinear material rods, the obtained corresponding transmission coefficients are shown in Subfigures (2) and (3), respectively.

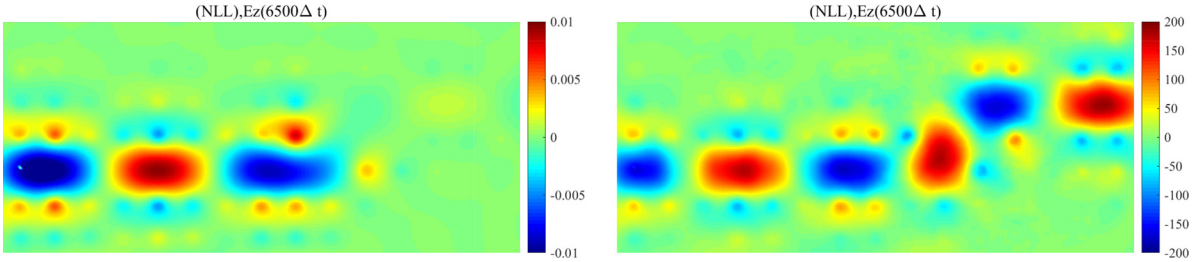

Fig. 6. The electric fields E_z obtained at time $t = 6500\Delta t$ for the Kerr-type nonlinear bent PCWG given in Fig. 5(a). The incoming waves are sine waves whose frequencies are $0.33c/a$, and intensities are 0.01 V/m (left) and 200 V/m (right), respectively. In this experiment, we also consider the triangle mesh, whose mesh size is $h = \frac{a}{12}$, and the time step size $\tau = \frac{h}{6c}$.

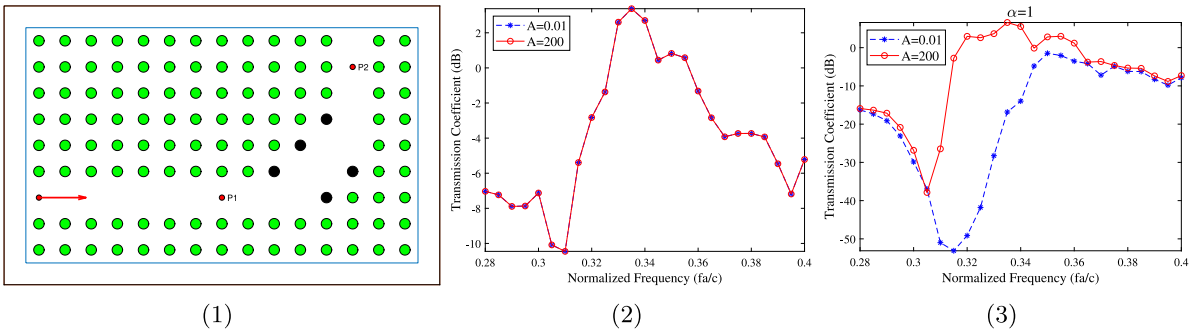

Fig. 7. Subfigure (1) is a L-shaped PCWG. In this experiment, we use the same incident waves as the experiment given in Fig. 3. Setting the black rods in Subfigure (1) as linear material rods and Kerr-type nonlinear material rods, the obtained corresponding transmission coefficients are shown in Subfigures (2) and (3), respectively.

can pass the bent Kerr-type nonlinear PCWGs well in the bistable frequency band, but the low-intensity waves cannot. Furthermore, when the electromagnetic wave, whose frequency is outside the bistable frequency band, passes through the bent Kerr-type nonlinear PCWG, the transmission coefficient is almost unaffected by the intensity of the electromagnetic wave. Therefore, by inserting several Kerr-type nonlinear material rods into the bend of linear PCWG, we can obtain a bistable transmission optical switch that depends on the intensity of the incoming wave. The optical switches can filter low-intensity waves, whose frequencies are in the bistable frequency band, which is related to the PBG of photonic crystal and the parameters of the Kerr-type nonlinear material rods.

Next, we introduce the experimental results of the bent Kerr-type nonlinear PCWGs formed by the triangular unit cells. The material parameters are the same as given above.

Figs. 9(b) and 10(b) show that in the waveguides composed of triangular unit cells, we can design a bistable transmission optical switch which depends on the incoming waves' intensities by using the same method.

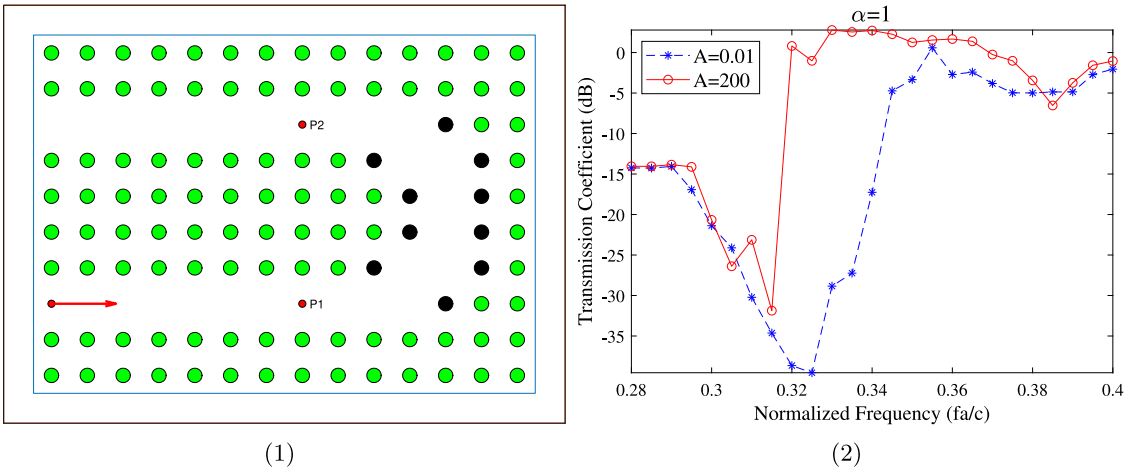

Fig. 8. Subfigure (1) is a U-shaped waveguide. In this experiment, we also use the same incident waves as the experiment given in Fig. 3. Setting the black rods in Subfigure (1) as Kerr-type nonlinear material rods, the obtained corresponding transmission coefficients are shown in Subfigure (2).

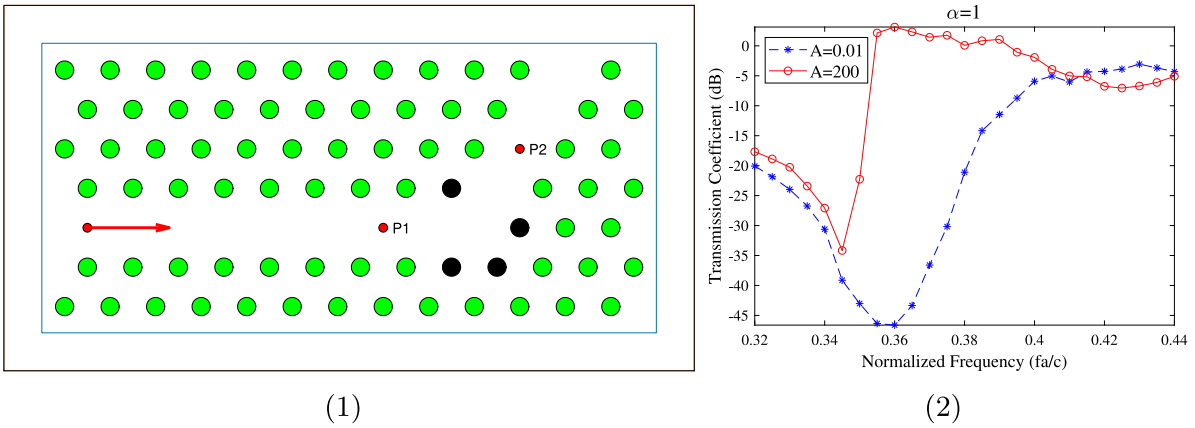

Fig. 9. Subfigure (1) is a V-shaped waveguide formed by triangular unit cells, and the black rods are made of Kerr-type material. In this experiment, we take $A = 0.01$ V/m, 200 V/m and frequencies in the range $(0.32c/a, 0.44c/a]$. Subfigure (2) shows the obtained transmission coefficient.

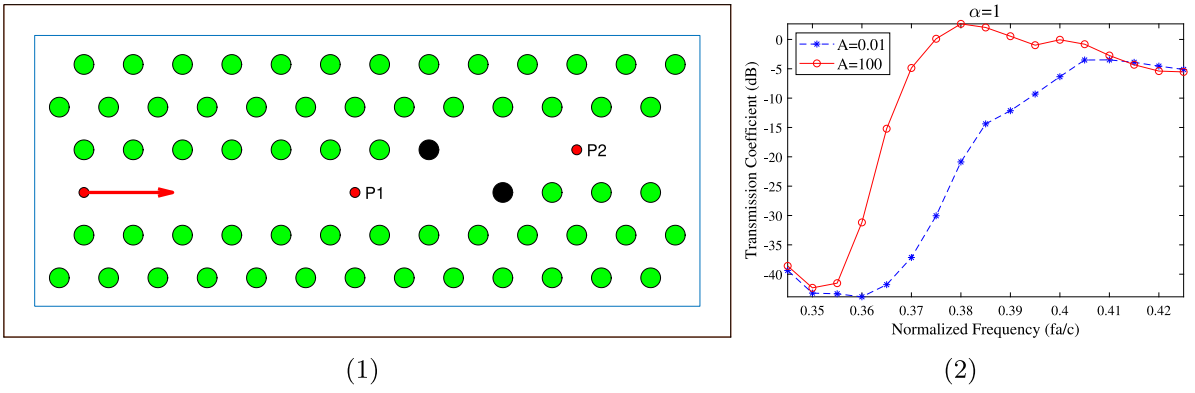

Fig. 10. Subfigure (1) is a Z-shaped waveguide formed by triangular unit cells, and the black rods are made of Kerr-type material. In this experiment, we take $A = 0.01$ V/m, 100 V/m and frequencies in the range $[0.345c/a, 0.425c/a]$. Subfigure (2) shows the calculated transmission coefficient.

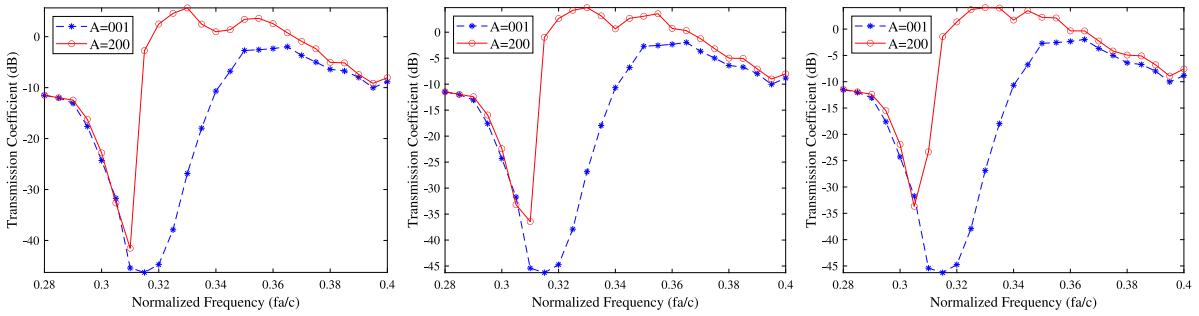

Fig. 11. The transmission coefficients obtained for the sine waves passing through the bent Kerr–Raman-type nonlinear PCWGs showed in Fig. 3(a) with $\alpha = 0, 0.3, 0.7$.

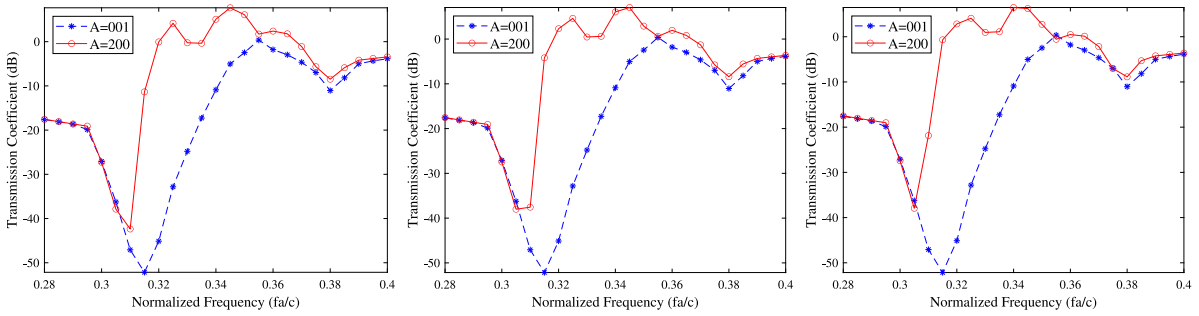

Fig. 12. The transmission coefficients obtained for the sine waves passing through the bent Kerr–Raman-type nonlinear PCWGs showed in Fig. 5(a) with $\alpha = 0, 0.3, 0.7$.

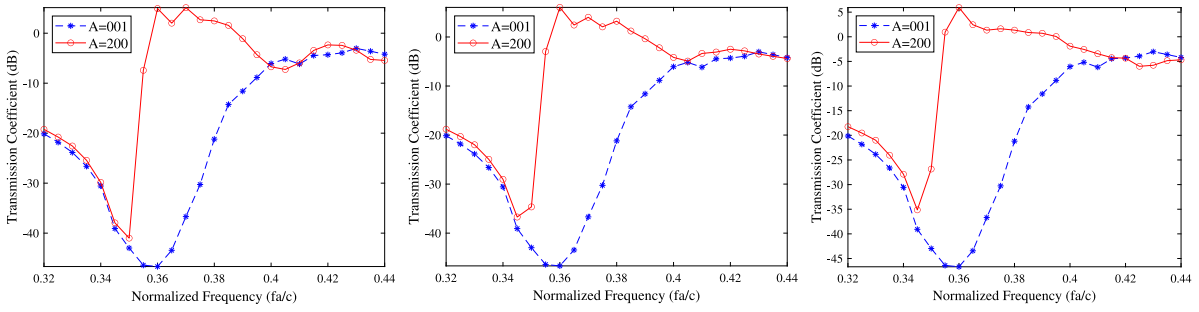

Fig. 13. The transmission coefficients obtained for the sine waves passing through the bent Kerr–Raman-type nonlinear PCWGs showed in Fig. 9(a) with $\alpha = 0, 0.3, 0.7$.

5.2. Kerr-Raman-type nonlinear PCWGs

Following [14,38], we take the function $g(t) = \alpha\delta(t) + (1-\alpha)g_R(t)$, where

$$g_R(t) = \tilde{A}\exp(-t/\tau_2)\sin(t/\tau_1)u(t), \quad \tilde{A} = \frac{\tau_1^2+\tau_2^2}{\tau_1\tau_2^2},$$

with $\tau_1 = 12.2$ femtosecond (fs) $= 12.2\cdot 10^{-15}$ s, $\tau_2 = 32$ fs, and $u(t)$ denotes the unit step function. In this case, the Fourier transform [14] can be used to obtain Eq. (9) with $a_1 = \frac{\tau_1}{\tilde{A}}$, $a_2 = \frac{2\tau_1}{\tilde{A}\tau_2}$, $a_3 = 1$, and the Z-transform [9] can be used to obtain the second-order difference Eq. (39).

Taking the waveguides in Figs. 3(a) 5(a) and 9(a) as examples, we simulate the propagation of sine waves passing through bent Kerr–Raman-type nonlinear PCWGs with $\alpha = 0, 0.3, 0.7$, respectively, where the sine waves have the same intensities and frequencies as those given in Figs. 3(c), 5(c) and 9(b). The obtained transmission coefficients are shown in Figs. 11–13, respectively.

From Figs. 11, 12, 13, 3(c), 5(c) and 9(b), we see that the bistable frequency band is related to α. When several rods made of Kerr–Raman-type, Raman-type or Kerr-type nonlinear materials are inserted into the bend waveguides, the bent PCWGs behave as bistable transmission optical switches which depend on the incoming waves' intensities.

6. Conclusion

In this paper, we prove the continuous stability of a kind of third-order nonlinear Maxwell's equations. Then we adopt the Cardano's method with our time-domain finite element scheme to solve the third-order nonlinear constitutive equation. We also prove the numerical stability of the FETD scheme for the Kerr–Maxwell's equations. Due to its complexity, we did not pursue the numerical stability and convergence analysis for the general third-order nonlinear Maxwell's equations. We hope that they can be established by following our previous work [18]. In the numerical experiment, we use the FETD scheme to simulate the propagation of sine waves through various bent waveguides. Our results show that bistable transmission switches depending on the intensity of the incident wave can be constructed by inserting some Kerr–Raman-type, Raman-type or Kerr-type nonlinear rods into the linear bend photonic crystal waveguides.

Data availability

Data will be made available on request.

Acknowledgments

The authors are grateful for two anonymous reviewers for their insightful comments on improving our paper.

Funding

Liu's work is supported by Postgraduate Scientific Research Innovation Project of Hunan Province (No. CX20210596) and Postgraduate Scientific Research Innovation Project of Xiangtan University (No. XDCX2021B102). Yang's work is supported by Hunan Outstanding Youth Fund (2022JJ10043), NSFC Projects 12171411 and 11771371. Li's work is supported by NSF grant DMS-2011943.

References

[1] E. Yablonovitch, Inhibited spontaneous emission in solid-state physics and electronics, Phys. Rev. Lett. 58 (1987) 2059.
[2] S. John, Strong localization of photons in certain disordered dielectric superlattices, Phys. Rev. Lett. 58 (1987) 2486.
[3] J.D. Joannopoulos, S.G. Johnson, J.N. Winn, R.D. Meade, Photonic Crystals: Molding the Flow of Light, Princeton University Press, Princeton, 2011.
[4] C. Ciminelli, Introduction to photonic crystals and metamaterials, in: A. Andreone, A. Cusano, A. Cutolo, V. Galdi (Eds.), Selected Topics in Photonic Crystals and Metamaterials, 2011, pp. 1–46.
[5] M.V. Rybin, D.S. Filonov, K.B. Samusev, P.A. Belov, Y.S. Kivshar, M.F. Limonov, Phase diagram for the transition from photonic crystals to dielectric metamaterials, Nature Commun. 6 (2015) 10102.
[6] A. Chutinan, S. Noda, Highly confined waveguides and waveguide bends in three-dimensional photonic crystal, Appl. Phys. Lett. 75 (1999) 3739–3741.
[7] M.M. Gilarlue, S.H. Badri, H.R. Saghai, J. Nourinia, Ch. Ghobadi, Photonic crystal waveguide intersection design based on Maxwell's fish-eye lens, Photon. Nanostruct.: Fundam. Appl. 31 (2018) 154–159.
[8] A. Mekis, J.C. Chen, I. Kurland, S. Fan, P.R. Villeneuve, J.D. Joannopoulos, High transmission through sharp bends in photonic crystal waveguides, Phys. Rev. Lett. 77 (1996) 3787.
[9] E.P. Kosmidou, T.D. Tsiboukis, An FDTD analysis of photonic crystal waveguides comprising third-order nonlinear materials, Opt. Quantum Electron. 35 (2003) 931–946.
[10] N. Kono, M. Koshiba, Three-dimensional finite element analysis of nonreciprocal phase shifts in magneto-photonic crystal waveguides, Opt. Express 13 (2005) 9155–9166.
[11] D. Boffi, M. Conforti, L. Gastaldi, Modified edge finite elements for photonic crystals, Numer. Math. 105 (2006) 249–266.
[12] M.A. Botchev, Krylov subspace exponential time domain solution of Maxwell's equations in photonic crystal modeling, J. Comput. Appl. Math. 293 (2016) 20–34.
[13] Z. Lu, A. Cesmelioglu, J.J.W. Van Der Vegt, Y. Xu, Discontinuous Galerkin approximations for computing electromagnetic Bloch modes in photonic crystals, J. Sci. Comput. 70 (2017) 922–964.
[14] M. Fujii, M. Tahara, I. Sakagami, W. Freude, P. Russer, High-order FDTD and auxiliary differential equation formulation of optical pulse propagation in 2-D Kerr and Raman nonlinear dispersive media, IEEE J. Quantum Electron. 40 (2004) 175–182.
[15] H. Jia, J. Li, Z. Fang, M. Li, A new FDTD scheme for Maxwell's equations in Kerr-type nonlinear media, Numer. Algorithms 82 (2019) 223–243.
[16] J. Huang, C.-W. Shu, A second-order asymptotic-preserving and positivity-preserving discontinuous Galerkin scheme for the Kerr-Debye model, Math. Models Methods Appl. Sci. 27 (2017) 549–580.
[17] A. Anees, L. Angermann, Energy-stable time-domain finite element methods for the 3d nonlinear maxwell's equations, IEEE Photonics J. 12 (2020) 1–15.
[18] Y. Huang, J. Li, B. He, A time-domain finite element scheme and its analysis for nonlinear Maxwell's equations in Kerr media, J. Comput. Phys. 435 (2021) 110259.
[19] M. Lyu, V. Bokil, Y. Cheng, F. Li, Energy stable nodal discontinuous galerkin methods for nonlinear maxwell's equations in multi-dimensions, J. Comput. Phys. 89 (2021) 45.
[20] J. Wang, Convergence analysis of an accurate and efficient method for nonlinear Maxwell's equations, Discrete Contin. Dyn. Syst. Ser. B 26 (5) (2021) 2429.

[21] E.T. Chung, P. Ciarlet Jr., A staggered discontinuous Galerkin method for wave propagation in media with dielectrics and meta-materials, J. Comput. Appl. Math. 239 (2013) 189–207.
[22] J. Li, C. Shi, C.-W. Shu, Optimal non-dissipative discontinuous Galerkin methods for Maxwell's equations in Drude metamaterials, Comput. Math. Appl. 73 (2017) 1760–1780.
[23] C. Shi, J. Li, C.-W. Shu, Discontinuous Galerkin methods for Maxwell's equations in Drude metamaterials on unstructured meshes, J. Comput. Appl. Math. 342 (2018) 147–163.
[24] J. Wang, J. Zhang, Z. Zhang, A CG–DG method for Maxwell's equations in Cole-Cole dispersive media, J. Comput. Appl. Math. 393 (2021) 113480, 19 pp.
[25] Y. Xie, L. Zhong, C. Liu, Convergence of an AEFEM for time-harmonic Maxwell equations with variable coefficients, J. Comput. Appl. Math. 372 (2020) 112712, 13 pp.
[26] H. Duan, W. Liu, J. Ma, R.C.E. Tan, S. Zhang, A family of optimal Lagrange elements for Maxwell's equations, J. Comput. Appl. Math. 358 (2019) 241–265.
[27] K. Li, T.-Z. Huang, L. Li, S. Lanteri, A reduced-order DG formulation based on POD method for the time-domain Maxwell's equations in dispersive media, J. Comput. Appl. Math. 336 (2018) 249–266.
[28] S. Descombes, S. Lanteri, L. Moya, Temporal convergence analysis of a locally implicit discontinuous Galerkin time domain method for electromagnetic wave propagation in dispersive media, J. Comput. Appl. Math. 316 (2017) 122–132.
[29] R.W. Boyd, Nonlinear Optics, Academic Press, 2020.
[30] J.C. Nédélec, Mixed finite elements in R^3, Numer. Math. 35 (1980) 315–341.
[31] J. Li, Y. Huang, Time-Domain Finite Element Methods for Maxwell's Equations in Metamaterials, in: Springer Series in Computational Mathematics, vol. 43, Springer-Verlag, Heidelberg, 2013.
[32] J.-P. Berenger, A perfectly matched layer for the absorption of electromagnetic waves, J. Comput. Phys. 114 (1994) 185–200.
[33] G. Bao, P. Li, H. Wu, An adaptive edge element method with perfectly matched absorbing layers for wave scattering by biperiodic structures, Math. Comp. 79 (2010) 1–34.
[34] E. Bécache, P. Joly, M. Kachanovska, V. Vinoles, Perfectly matched layers in negative index metamaterials and plasmas, ESAIM Proc. Surv. 50 (2015) 113–132.
[35] J.L. Hong, L.H. Ji, L.H. Kong, Energy-dissipation splitting finite-difference time-domain method for Maxwell equations with perfectly matched layers, J. Comput. Phys. 269 (2014) 201–214.
[36] M. Chen, Y. Huang, J. Li, Development and analysis of an new nite element method for the Cohen-Monk PML model, Numer. Math. 147 (2021) 127–155.
[37] S.D. Gedney, An anisotropic perfectly matched layer-absorbing medium for the truncation of FDTD lattices, IEEE Trans. Antennas and Propagation 44 (1996) 1630–1639.
[38] K.J. Blow, D. Wood, Theoretical description of transient stimulated Raman scattering in optical fibers, IEEE J. Quantum Electron. 25 (1989) 2665–2673.